Supplemental Information: Electrical Characterization of Discrete Defects and Impact of Defect Density on Photoluminescence in Monolayer WS_2

Matthew R. Rosenberger, Hsun-Jen Chuang, Kathleen M. McCreary, Connie H. Li, and Berend T. Jonker**

Naval Research Laboratory, Washington, DC 20375, USA

**Corresponding Author Emails:* matthew.rosenberger.ctr@nrl.navy.mil, berry.jonker@nrl.navy.mil

Details of Sample Preparation

In our measurements, we are interested in understanding the material properties of the TMD monolayer. However, the current measured with conductive AFM depends on both the intrinsic TMD monolayer properties and external factors, such as the presence of wrinkles, bubbles, and contaminants on top of or underneath the monolayer. In order to isolate the TMD intrinsic properties, it is important to limit variations of these external factors across the sample. As a result, sample preparation is critical for performing useful and repeatable conductive AFM measurements on TMD monolayers. In particular, the substrate should be as flat as possible and the TMD film should be free of wrinkles, bubbles, and contaminants.

To achieve a flat, conductive substrate, we exfoliated graphite onto a thin layer of Ti/Au, which we evaporated onto a Si wafer. The Ti/Au layer allowed for easy electrical contact. Using a PDMS stamp, we picked up CVD grown WS_2 grains and transferred them onto the exfoliated graphite. After transfer, the sample had considerable wrinkles and evidence of contaminants trapped between the WS_2 and the graphite [**Figure S1(a)**]. Using an AFM tip in contact mode, we flattened out several regions on the WS2 grain in order to remove the wrinkles/contaminants and improve the uniformity of contact between the WS_2 and graphite [**Figure S1(b)**]. Without

flattening the WS_2 layer, the conductive AFM results are ambiguous because they represent a convolution of intrinsic material properties and external perturbations, such as changes in height [**Figure S2**]. Such results are not useful for defect characterization because we cannot decouple the intrinsic and extrinsic effects.

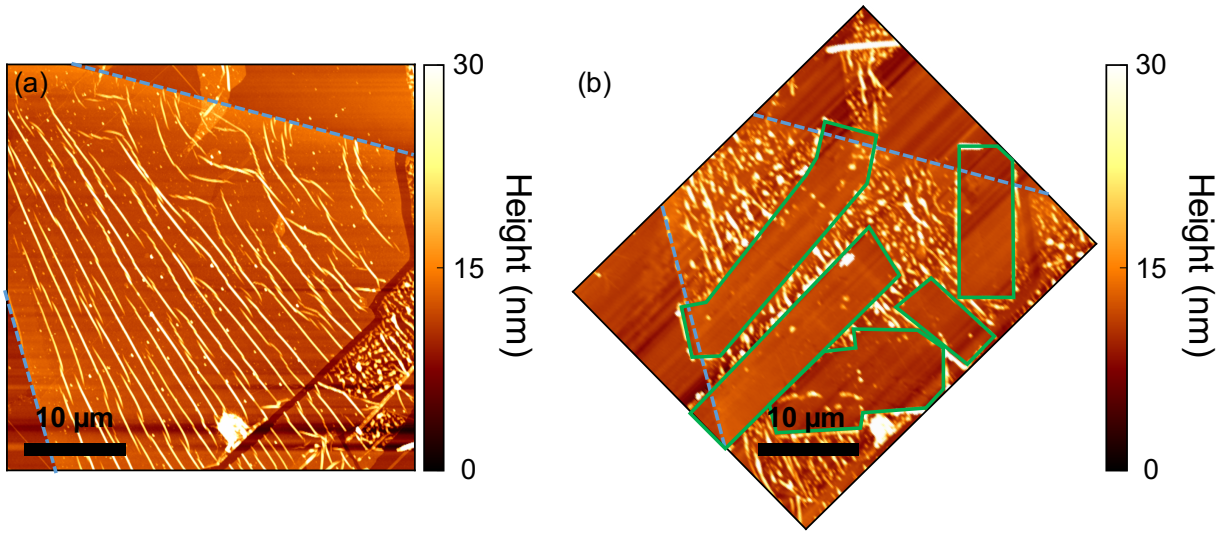

Figure S1. Comparison of AFM topography of WS_2 after transfer onto graphite (a) before AFM flattening and (b) after AFM flattening. The blue dashed lines show the edges of the WS_2 triangle. The regions outlines in green are the regions that were flattened with AFM. The flattened regions show much better uniformity and flatness, which is essential for consistent and repeatable CAFM measurements.

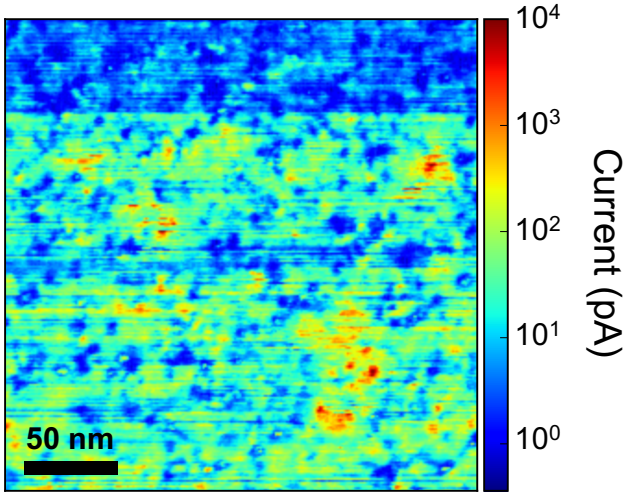

Figure S2. Conductive AFM measurement taken on an unflattened region of WS_2. The nonuniformity of the contact between WS_2 and graphite leads to ambiguous results and an inability to identify defect locations. Sample bias for this measurement was 1 V.

Different AFM Tips Locate the Same Defects

The observed shape of defects in conductive AFM measurements are slightly different depending on the particular AFM tip used for the measurement due to the inherent variations in tip shape for different AFM tips. However, as seen in **Figure S3**, different AFM tips identify the same defects, indicating that these measurements can be used to accurately observe defect locations and to quantify defect density.

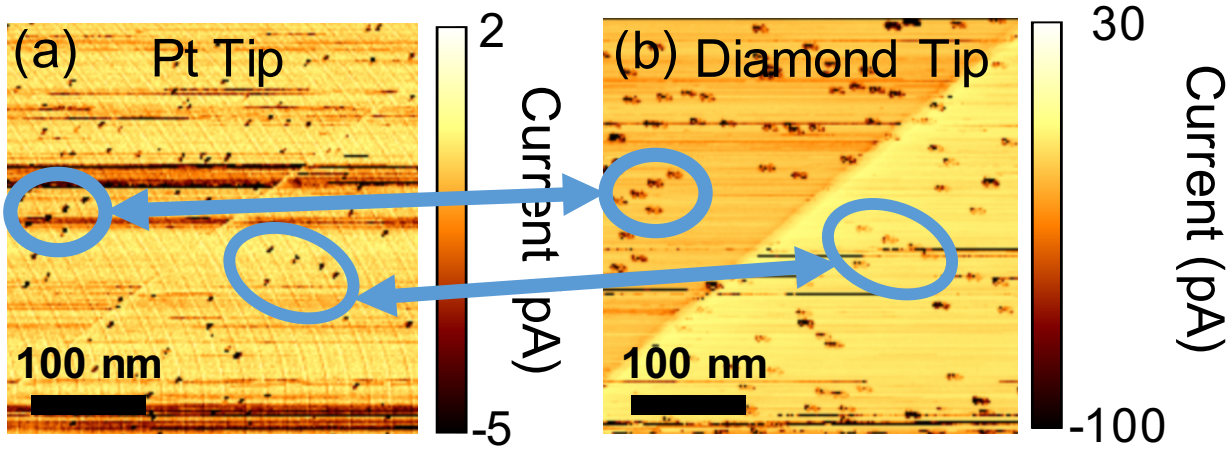

Figure S3. Demonstration that different tips locate the same defects despite having different tip shapes, and, therefore, different observed defect shapes. (a) Conductive AFM measurement of WS_2 defects with a Pt coated AFM tip. (b) Conductive AFM measurement of WS_2 defects with a diamond coated AFM tip. The blue circles are guides to the eye showing two clusters of defects. Sample bias was -1.2 V for (a) and -1.5 V for (b).

Estimating Defect Size from Conductive AFM

Figure S4 shows our estimation of the defect radius from conductive AFM measurements. It is extremely difficult to precisely determine the exact size of the tip-sample contact in order to deconvolute and deduce the exact defect size and shape. Instead, we use the observed defect size as the estimated defect size, as shown in **Figure S4** of a high resolution image of an isolated defect. In this image, the apparent defect dimension is 4.88 nm in one direction and is 2.34 nm

in the perpendicular direction. Assuming that the defect should be approximately circular/symmetric and the asymmetry arises from the irregular shape of the tip-sample contact, we use the smaller value of 2.34 nm as the defect diameter, which results in an estimated defect radius of 1.2 nm. We believe that this is a reasonable estimate, particularly since the observed defect size should be an upper limit on the actual defect size due to the finite size of the tip-sample contact.

Regarding the AFM tip size, even though the typical tip radius is ~20nm, 10 times that of the defect, the tip-sample contact is likely much smaller than the tip radius, since AFM tips can have nanoscopic asperities that determine the tip-sample contact size and shape. Hence, AFM tips should be able to resolve features that are much smaller than the tip radius, similar to the subatomic resolution routinely achieved using STM tips with a much larger tip radius. Furthermore, our measured defect radius of 1.2 nm is also comparable to previous STM measurements of TMD defects.[1]

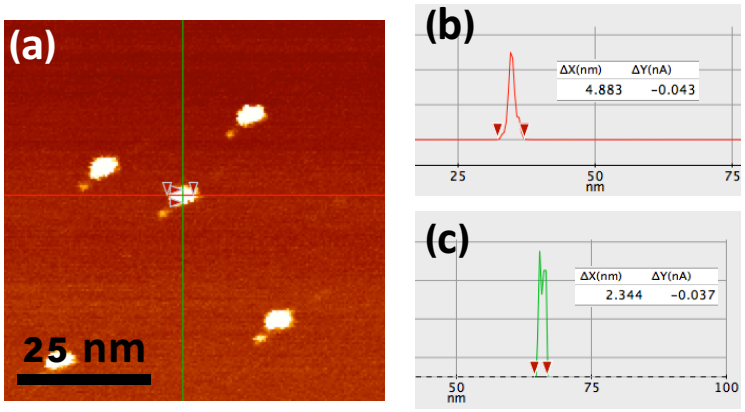

Figure S4. Estimation of defect size. (a) Conductive AFM map of 5 defects. (b) Measurement of apparent defect size in x-direction is 4.88 nm. (c) Measurements of apparent defect size in y-direction is 2.34 nm. We expect that the measurement is a convolution of the tip shape in the particular direction and the defect size. We chose to use the smaller of the two measurements as an estimate of the defect size. This estimate is an upper limit on the real size of the defect because this measurement likely has some broadening due to the AFM tip width in the y-direction.

Detailed Derivation of Exciton Recombination Model

The base assumption of our model is that the material is in steady state (CW laser experiments), which means that the exciton generation rate, $\dot{N}_{gen} = \frac{1}{\tau_{gen}}$, is equal to the exciton recombination rate, $\dot{N}_{rec} = \frac{1}{\tau_{rec}}$. Exciton recombination occurs via several parallel radiative and non-radiative processes. In this work, we assume that there is one radiative recombination process with $\dot{N}_r = \frac{1}{\tau_r}$, one non-radiative recombination process that depends on defects with $\dot{N}_{nr,def} = \frac{1}{\tau_{nr,def}}$, and one non-radiative recombination process related to sample/substrate interaction with $\dot{N}_{nr,sub} = \frac{1}{\tau_{nr,sub}}$. $\dot{N}_{nr,sub}$ may also include any other intrinsic or extrinsic non-radiative recombination mechanisms that are not associated with defects. With these definitions, Eqn. (S1) represents the exciton conservation equation for excitons in steady state:

$$\frac{1}{\tau_{gen}} = \frac{1}{\tau_r} + \frac{1}{\tau_{nr,sub}} + \frac{1}{\tau_{nr,def}}. \quad \text{(S1)}$$

The quantum yield (QY) of the material is defined by Eqn. (S2):

$$QY = \frac{\frac{1}{\tau_r}}{\frac{1}{\tau_r} + \frac{1}{\tau_{nr,sub}} + \frac{1}{\tau_{nr,def}}}. \quad \text{(S2)}$$

In this work, we assume that $\tau_r = 1.5\ nsec$,[2] as determined for material grown under the same conditions and in the same equipment as our previous work.

Photoluminescence Characterization of WS_2 on Graphite

Figure S5(a) shows a spatial map of PL signal for WS_2 on PDMS (same data as **Figure 5(a)**) and **Figure S5(b)** shows a spatial map of PL signal for the same WS_2 triangle after transfer onto graphite and subsequent AFM flattening. Note that the maximum intensity and dynamic range

in PL intensity for **Figure S5(a)** are 1000 times larger than that in **Figure S5(b)** due to strong quenching of the PL for WS_2 on graphite. The black dots labeled in the maps show the locations of CAFM measurements used for fitting the model to our experiments. The PL data have been scaled to account for a difference in power (5 µW for **Figure S5(a)** and 29 µW for **Figure S5(b)**) and acquisition time at each pixel (0.2 sec for **Figure S5(a)** and 1 sec for **Figure S5(b)**). Larger power and longer acquisition were necessary for **Figure S5(b)** in order to obtain sufficient signal-to-noise ratio. We did not observe a significant nonlinear response in PL signal, which indicates that comparing the scaled PL spatial maps is valid.

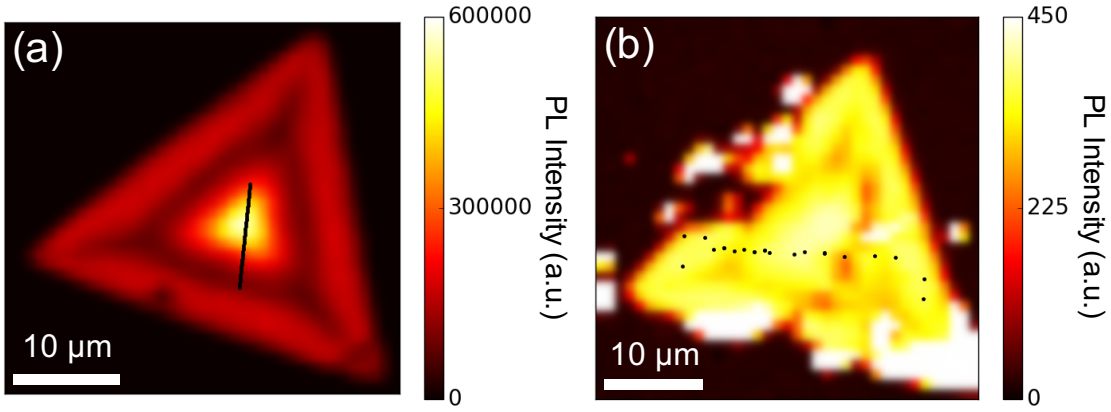

Figure S5. (a) Spatial map of photoluminescence intensity of a WS_2 grain (a) on PDMS and (b) on graphite. Locations of data used for fitting the experiment with the model are shown as black dots.

Potential Role of Adsorbates

To rule out the possibility that the high current features are simply adsorbates, we present the following points. In the absence of defects, adsorbates would be expected to randomly distribute on the surface with a uniform density across the WS_2 flakes. However, we have observed a distinct spatial dependence of the defect density across the WS_2. In addition, we

would expect random adsorbates to migrate over time. However, the precise locations of the defects we observe do not vary over time, as shown in Figure S3 where two images of the same area show the same defect locations, with more than 2.5 hours between the measurements.

We cannot rule out the possibility that adsorbates selectively adsorb to intrinsic defect sites. However, in this case, our measurements still identify the locations of intrinsic defects, hence our approach and conclusions are valid even if adsorbates are selectively adsorbed to intrinsic defect sites.

Do sample preparation and/or measurements introduce defects?

We have conducted PL measurements on many WS_2 flakes and have not observed any significant dependence of the PL intensity on laser power for the range of laser power used in this work. This suggests that the laser power used in this study likely did not damage the samples.

While we cannot definitively determine if the transfer of WS_2 onto graphite introduced any defects, we regularly observe that the PL intensity pattern is the same before and after transfer, suggesting that the transfer is not the dominant source of defects that are responsible for the PL intensity pattern.

We have done AFM flattening on WS_2 flakes on insulating substrates such as hBN (as not to quench the PL), and did not observe a significant change in the PL intensity before and after AFM flattening, indicating that AFM flattening does not substantially damage the WS_2. We would expect similar results for AFM flattening done on graphite substrates.

Furthermore, any defects that PL laser exposure, transferring, and AFM flattening may possibly introduce are expected to be uniform across the entire WS_2 flake, and would not be

responsible for the PL intensity pattern observed, which is only correlated with the observed high conductivity defects.

Regarding applied voltage during imaging, we have scanned the same locations many times using different voltages (typically ranging from 0 – 1 V) and have never observed the creation of new high conductivity defect-like features. Hence, we can conclude that the voltages used in this study do not introduce additional defects.

Circular Polarization in WS_2

Our results are consistent with our recent work that shows that circular polarization is inversely related to PL intensity.[2] Figure S6(a) shows the PL intensity and degree of circular polarization for a linescan across the middle of the WS_2 triangle on graphite [Figure S5(b)]. The PL intensity peak near the center of the grain corresponds to a drop in circular polarization. Figure S6(b) shows the degree of circular polarization as a function of PL intensity. Similar to our previous results, here we also observe an inverse relationship between circular polarization and PL intensity. This is consistent with our finding that in samples with lower PL intensity and higher defect density, the electrically active defects act as scattering centers that lead to short non-radiative lifetimes and, in turn, higher spin polarization by limiting opportunities for depolarizing scattering events.

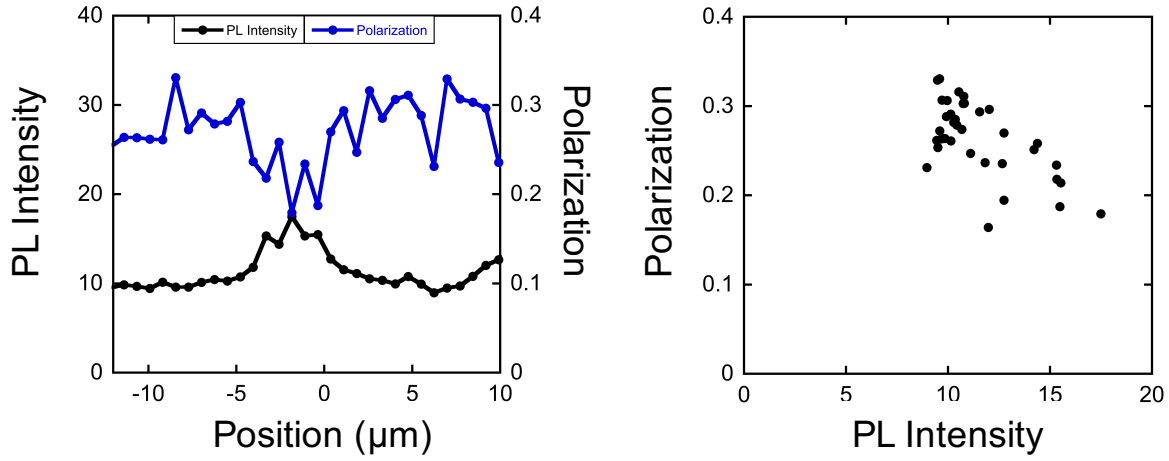

Figure S6. (a) PL intensity and circular polarization as a function of position for a linescan across the triangle after transfer to graphite and subsequent AFM flattening [Fig. S5(b)]. (b) Polarization as a function of PL intensity.

References

(1) Addou, R.; Colombo, L.; Wallace, R. M. Surface Defects on Natural MoS_2. *ACS Appl. Mater. Interfaces* **2015**, *7*, 11921–11929.

(2) McCreary, K. M.; Currie, M.; Hanbicki, A. T.; Chuang, H.-J.; Jonker, B. T. Understanding Variations in Circularly Polarized Photoluminescence in Monolayer Transition Metal Dichalcogenides. *ACS Nano* **2017**.